RSC Advances

PAPER

View Article Online
View Journal | View Issue

Cite this: *RSC Adv.*, 2020, **10**, 37072

Synthesis of CdS-loaded $(CuC_{10}H_{26}N_6)_3(PW_{12}O_{40})_2$ for enhanced photocatalytic degradation of tetracycline under simulated solar light irradiation†

Feng Li,[ac] Zhuomin Qiang,[a] Shunqiang Chen,[a] Jianyu Wei,[*b] Taohai Li[ac] and Dabin Zhang[d]

Largely discharged and excreted medical pollutants pose huge threats to ecosystems. However, typical photocatalysts, such as the Keggin-typed $H_3PW_{12}O_{40}$, can hardly degrade these hazards under visible-light due to their broad bandgap and catalytic disability. In this work, the visible light harvesting was enabled by combining macrocyclic coordination compound $CuC_{10}H_{26}N_6Cl_2O_8$ with $H_3PW_{12}O_{40}$, and the resulting CuPW was loaded with CdS to reach robust catalytic ability to totally detoxify medicines. We prepared the CuPW–CdS composites through a facile precipitation method, and it showed excellent photocatalytic degradation for degrading tetracycline under visible-light irradiation. The $(CuC_{10}H_{26}N_6)_3(PW_{12}O_{40})_2$ with 10 wt% load of CdS shows the highest performance and is ~6 times more efficient than the pure CuPW counterpart. The heterojunctional CuPW–CdS composites promote the separation of electrons and holes, and consequentially enhance photocatalytic activity. Thanks to migration of electrons from CdS to CuPW, the photocorrosion of CdS is prohibited, resulting in a high chemical stability during photocatalysis. In this work we design a new route to the multi-structural composite photocatalysts for practical applications in medical pollutant decontamination.

Received 26th April 2020
Accepted 18th September 2020

DOI: 10.1039/d0ra03755a

rsc.li/rsc-advances

1. Introduction

The discovery and utilization of tetracycline (TC) have improved human living standard thanks to its antibiotic functionalities and low clinical toxicity. However, its negative impact in bone development brings awareness of usage restriction in the human body. Nevertheless, cheap antibiotics are widely employed as additives in animal forage as well as medicine in many developing countries. Consequentially, the residual or excreted tetracycline turns up in meat products, surface water, sewage, soil, *etc.* Wide exposure to tetracycline can lead to antibiotic resistance in the human body and serious danger to bones.[1–3] Thus, effective and cheap decontamination methods are needed to remove this manmade chemical from nature.

So far, various water treatment techniques have been developed to remove medical wastes and organic dyes in wastewater. Typical cleanteches can be branched as physical adsorption,[4–7] biological removal,[8,9] chemical degradation.[10–13] Among these, chemical degradation of dye and antibiotic is considered as an effective solution.[14–16] As a typical chemical process, semiconductor photocatalysis distinguishes itself from other peers due to environmental friendliness, renewable utilization, and low cost.[17–20] For instance, the photocatalytic degradation of TC can be performed with existence of thickness-controllable $Bi_{24}O_{31}Br_{10}$.[21] Perovskite oxide/g-C_3N_4 photocatalysts were also developed, and a degradation rate of 81% was reached.[22] And the latest reports on the conventional photocatalysts for different photocatalytic applications are summarized in Table S1.† Despites these progresses, the highly toxic by-product have produced in the photocatalytic process of TC. Four stable aromatic rings within these products hinder the further degradations. Moreover, conventional photocatalysts suffer from easy decomposition and non-activity under visible light/sunlight irradiation, yet, hardly work outside lab.[23–25] Therefore, it is urgently desired to develop novel visible-light photocatalysts which can open aromatic rings while maintain chemical stability against photocorrosion.

Polyoxometalates (POMs) belong to an emerging group of semiconductor photocatalysts. They are endowed with unique magnetic,[26] redox,[27] and catalytic properties[28,29] thanks to fast electron–hole pair separation processes. However, lack of visible-light adsorption and easy aqueous dissolution limit its photocatalytic applications in practical ambiences. Engineering semiconductive heterojunctions can extend light absorption

[a]College of Chemistry, Key Lab of Environment Friendly Chemistry and Application in Ministry of Education, Xiangtan University, Xiangtan, 411105, China
[b]China Tobacco Guangxi Industrial Co., Ltd, Nanning, Guangxi 530001, PR China. E-mail: jtx_wjy@163.com
[c]Nano and Molecular Systems Research Unit, Faculty of Science, University of Oulu, P.O. Box 3000, FIN-90014, Finland
[d]School of Mechanical Engineering, Guizhou University, Guiyang, Guizhou 550025, PR China

† Electronic supplementary information (ESI) available. See DOI: 10.1039/d0ra03755a

range, promote catalytic ability and bolster chemical stability.[30,31] In this regard, the cadmium sulfide (CdS) is a good heterojunctional part due to its solar radiance acceptance,[32] redox potential and high efficiency separation of photoinduced electron–hole pairs.[33] Despites these merits, the CdS suffers from easy photocorrosion due to the positively charged holes can oxidize S^{2-} ions to S^0 phase.[34,35] Therefore, it is generally important to improve the separation efficiency of photoinduced electron–hole pairs, thus enhancing the stability of cadmium sulfide in photocatalysis.[36,37] Taking the materials properties of the $H_3PW_{12}O_{40}$ and CdS, a combination of POM–CdS may become a promising photocatalytic heterojunction for practical tetracycline pollutant decontamination under visible light radiation.

In this work, we demonstrate an incorporation of a Keggin-type $H_3PW_{12}O_{40}$ into the $(CuC_{12}H_{30}N_6)^{2+}$ by a simple one-pot self-assembly process to overcome unfavorable visible light response and easy aqueous dissolution under light irradiation. Novel CuPW–CdS composites were successfully prepared through water bath synthetic strategy. CuPW–CdS composites showed remarkable visible-light photocatalytic degradation activity for TC and also for model pollutants such as RhB. Photocatalytic mechanism in the heterojunctional complexes was also explored. Besides reaching an efficient complex for medical pollutant decontamination, the work is hoped to debut a universal route in synthesis of POM-based photocatalysts for robust chemical activity and reusability in practical applications.

2. Experimental

2.1 Materials and synthesis

Chemicals involved in the synthesis are methanol, $CuCl_2 \cdot 2H_2O$, ethylenediamine, formaldehyde, methylamine, perchloric acid, cadmium chloride hemi (pentahydrate) ($CdCl_2 \cdot 2.5H_2O$), sodium sulfide (Na_2S), isophthalic acid (IPA).

The synthesis was performed in 2 steps. First, macrocyclic coordination compound (MCC) of $CuC_{10}H_{26}N_6Cl_2O_8$ was prepared to modify the polyoxometalates of the $H_3PW_{12}O_{40}$, yielding the MCC-POM reagent as a part in the photocatalysts. Later, the CdS was introduced to the MCC-POM to prepare the heterojunction photocatalysts.

2.2 Synthesis of $(CuC_{10}H_{26}N_6)_3(PW_{12}O_{40})_2$

Synthesis of $CuC_{10}H_{26}N_6Cl_2O_8$. $CuCl_2 \cdot 2H_2O$ (8.5 g) was added with 50.00 mL of methanol solution, ethylenediamine (6.80 mL), formaldehyde (20.00 mL), and methylamine (8.60 mL). The solution was heated at reflux for 24 h. Excess perchloric acid was added to the solution. The purple-red crystals were collected, washed with methanol, and recrystallized from hot water. Anal. calcd for $CuC_{10}H_{26}N_6Cl_2O_8$, C, 24.37; H, 5.32; N, 17.05. Found: C, 24.40; H, 5.37; N, 16.98.

Synthesis of $(CuC_{10}H_{26}N_6)_3(PW_{12}O_{40})_2$. In a typical procedure, 0.79 g $CuC_{10}H_{26}N_6Cl_2O_8$ and 2.88 g $H_3PW_{12}O_{40}$ were dissolved in 30 mL of distilled water by stirring at 50 °C for 1 h. After that, the pink precipitate was washed by water and ethanol, and then vacuum dried at 50 °C for 24 h. According to the previous research of other colleagues in the same research group, the possible chemical structure of $(CuC_{10}H_{26}N_6)_3(PW_{12}O_{40})_2$ has been proposed in Fig. S1,† consisting of two $PW_{12}O_{40}^{3-}$ and three $CuC_{10}H_{26}N_6^{2+}$.[38]

2.3 Synthesis of $(CuC_{10}H_{26}N_6)_3(PW_{12}O_{40})_2$–CdS composites

The CdS decorated $(CuC_{10}H_{26}N_6)_3(PW_{12}O_{40})_2$ nanoparticles were prepared by a water bath synthesis. In a typical preparation, 1.0 g of $(CuC_{10}H_{26}N_6)_3(PW_{12}O_{40})_2$ was dispersed in 20 mL distilled water and stirred 1 h at room temperature. Then 0.346 mmol Na_2S and 0.346 mmol $CdCl_2 \cdot 2.5H_2O$ were added into the beaker. After that, the power was recovered through washed by water and ethanol, and then dried at 60 °C for 12 h. The $(CuC_{10}H_{26}N_6)_3(PW_{12}O_{40})_2$–CdS composites were prepared with various mass ratio of $(CuC_{10}H_{26}N_6)_3(PW_{12}O_{40})_2$ and CdS, which were denoted as CuPW–CdS-0, CuPW–CdS-5, CuPW–CdS-10 and CuPW–CdS-15. The mass ratios of CuPW and CdS were 1 : 0.00, 1 : 0.05, 1 : 0.10 and 1 : 0.15, respectively.

2.4 Characterization

The powder X-ray diffraction (XRD) measurements were performed on a Rigaku Dmax/Ultima IV diffractometer. Morphological determinations were performed on a Scanning Electron Microscope (SEM, JSM-6610LV) and a transmission electron microscope (TEM, FEI Tecnai G20). X-ray photoelectron spectroscopy (XPS) measurements of samples were recorded on a PerkinElmer PHI 5000C spectrometer. The Fourier transform infrared (FTIR) spectroscopy was carried on a Nicolet 6700 FTIR Spectrometric. Photoluminescence (PL) spectroscopy was performed on a LS55 fluorescence spectrometer and excitation wavelength at 485 nm. UV-vis diffuse reflectance spectra of the samples were obtained from a UV-vis spectrophotometer (UV-2550, Japan).

2.5 Electrochemical measurements

To measure the electrochemical performance of composites, we prepare the working electrode by as-prepared sample were dispersed into ethanol and then the 10 μL of dispersion was drop-casted onto FTO with coated area of 1×1 cm^2. The electrochemical measurement was carried out an electrochemical workstation (CHI650D, CH Instruments Inc, Shanghai) in a typical three-electrode setup with an electrolyte solution of 0.5 M Na_2SO_4.

2.6 Photocatalytic measurements

The photocatalytic ability of CuPW–CdS was evaluated by the tetracycline (TC) degradation in aqueous solution and cross-checked with degradation of the model dye of rhodamine B (RhB) under light irradiation. The photocatalytic degradation experiments were carried out in a 250 mL of cylindrical quartz using a 500 W Xe arc lamp as radiation source. Typically, 100 mg of photocatalyst was added into 100 mL of 10 mg L^{-1} RhB or 10 mg L^{-1} tetracycline aqueous solution. Before the photocatalytic degradation experiment, the adsorption–desorption

equilibrium experiment is necessary. In the photocatalytic experiment, the suspension was centrifuged to take the supernatant at predetermined time intervals. The solution concentration left were tested by an UV-vis spectrophotometer (cary-60, Agilent) through checking its characteristic absorbance at 553 nm of RhB and 357 nm of TC.

The stability of the photocatalysts was examined by the recycling tests (four runs). After each run, the photocatalysts were collected by centrifuged and washed for three times, and finally dried at a temperature of 70 °C in an oven.

Moreover, in order to explore the role of active species in the photocatalytic process, the experiments of radicals capture were carried out. The influence of active species to the photocatalytic degradation of tetracycline was investigated by adding 1 mM of isopropyl alcohol (IPA), ammonium oxalate (AO), 1.4-benzoquinone (BQ) as scavengers to detect hydroxyl radical ($^{\bullet}OH$), hole (h^{+}) and superoxide radicals ($^{\bullet}O_2^{-}$), respectively before photodegradation experiment.

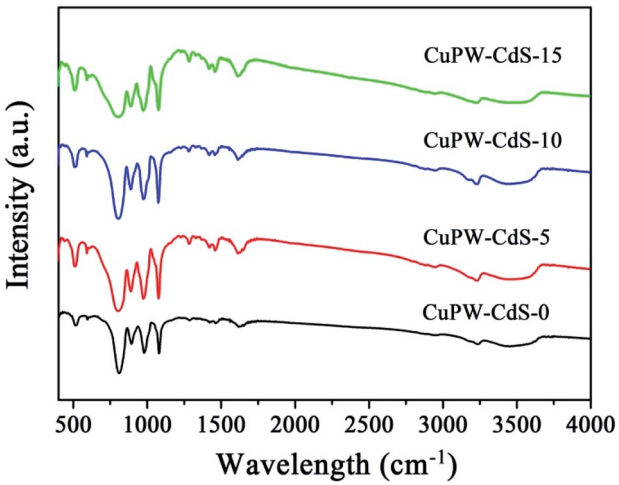

Fig. 2 FTIR spectra of CuPW–CdS-0, CuPW–CdS-5, CuPW–CdS-10 and CuPW–CdS-15 samples.

3. Results and discussion

3.1 Characterization of as-prepared photocatalysts

Fig. 1 depicts typical X-ray diffraction (XRD) patterns of CuPW–CdS-0, CuPW–CdS-5, CuPW–CdS-10, CuPW–CdS-15 and CdS. The diffraction peaks of CuPW–CdS samples match well with the CuPW–CdS-0, denoting high purity and crystallinity of the heterojunction. No shift was observed in the peak positions of CuPW patterns compared to these of CuPW–CdS. The load of CdS with CuPW did not destroy the morphology and crystallinity of the substrate. There are three peaks at 2θ value of 24.86, 25.28 and 28.28 can be indexed to (400), (040), (240) plane diffraction of CdS (JCPDS no: 47-1179). Furthermore, for the XRD pattern of CuPW–CdS-5, CuPW–CdS-10, CuPW–CdS-15, the XRD pattern of CdS was no obviously in composites, which can be ascribed to the little amount of CdS and the lower XRD peaks of CdS.[39]

The functional group of the CuPW–CdS samples was studied by FTIR spectroscopy in Fig. 2. Characteristic bands at 3239 and 1617 cm^{-1} were ascribed to νN–H and νC=C stretching vibration, respectively.[38] Bands at 1465 and 1286 cm^{-1} belong to methyl. The PW_{12} showed four characteristics bands at 1080 (P–O_a), 979 (W=O_d), 894 (W–O_b–W), and 810 (W–O_c–W) cm^{-1}.[40] This indicates the new compound has been successfully prepared, in line with the XRD results.

The morphology features of pure CuPW flakes and CdS nanoparticles were shown in Fig. S2a and b.† The TEM image of pure CuPW exhibited irregular nanosheet structure and smooth surface, CdS presented simultaneously nanoparticles with a particle size of 10 nm. The SEM image of CuPW–CdS-10 was depicted in Fig. 3a. No clear traces of CdS nanoparticles could be observed in the SEM images due to low concentration and small sizes compared with the CuPW. Through the TEM images in Fig. 3b–d, the CdS nanoparticles were found closely contact

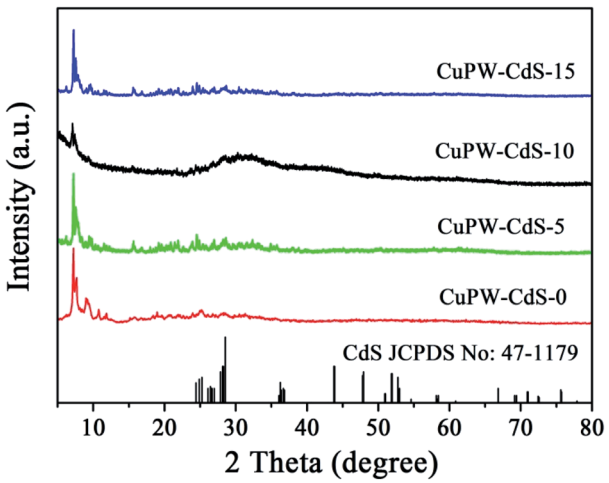

Fig. 1 XRD patterns of CuPW–CdS-0, CuPW–CdS-5, CuPW–CdS-10 and CuPW–CdS-15 samples.

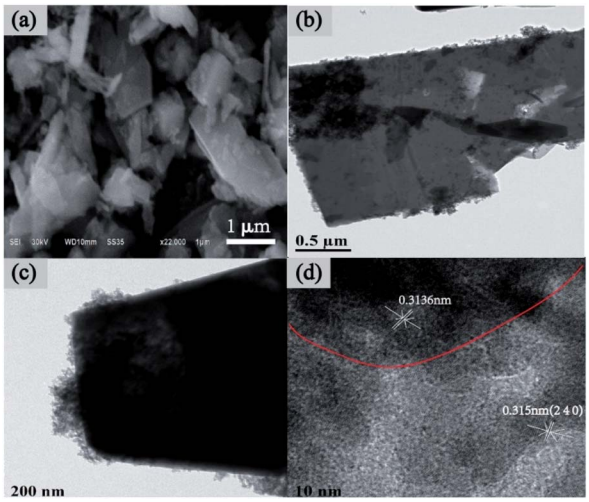

Fig. 3 (a) SEM image of CuPW–CdS-10. (b–d) TEM images and HRTEM image of CuPW–CdS-10.

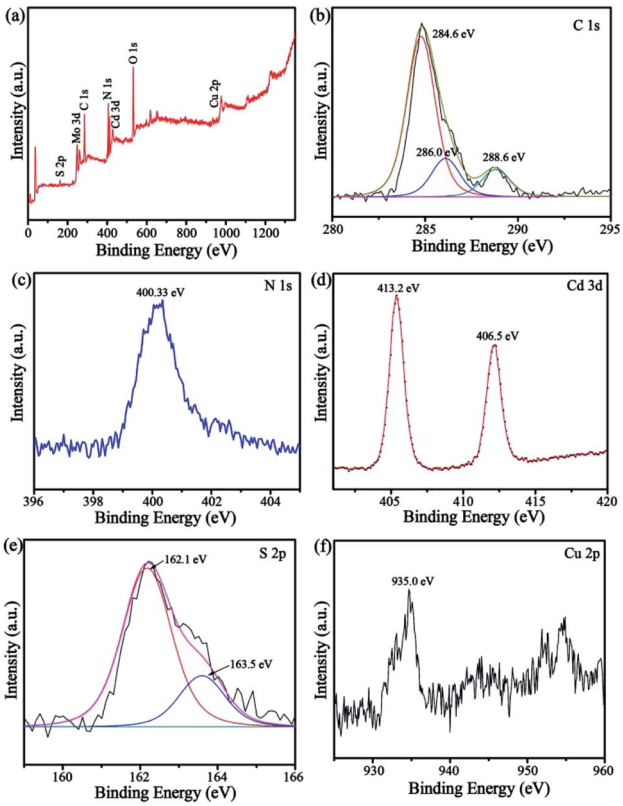

Fig. 4 XPS patterns of the CuPW–CdS-10: (a) survey, (b) C 1s, (c) N 1s, (d) Cd 3d, (e) S 2p and (f) Cu 2p.

with CuPW flakes following the interaction between CuPW and CdS counterparts (Fig. 3b and c). The HRTEM image of CuPW–CdS-10 shows in Fig. 3d, the lattice spacing of 0.3136 nm of the CuPW flakes and the CdS nanoparticles with lattice spacing of 0.315 nm is consistent with the (240) lattice plane, respectively. Furthermore, in Fig. S2e–j,† EDX mapping of CuPW–CdS-10 heterostructure reveals the presence of Cd, S, Cu, P and W in the whole selected region, suggesting the uniform dispersion of the elements. It can be clearly observed that CdS agglomerated on the surface of CuPW when CdS increased to 15%, which may reduce the photocatalytic active sites. According to the above mentioned, combined with XRD and FTIR results, it can be deduced that CdS is exactly covered with CuPW.

The survey XPS spectrum (Fig. 4a) demonstrated that CuPW–CdS composites were composed of C, N, S, Cd and Cu elements. The high-resolution C 1s XPS spectrum (Fig. 4b) shows binding energies of 284, 286, and 288.6 eV for C. These are characteristics of C–C, N=C–N and π-excitation bonding in CuPW–CdS, respectively.[41] In the N 1s spectrum (Fig. 4c), the peak at 400.33 eV can be attributed to the C–N=C.[42] In Fig. 4d, the Cd 3d peaks at 406.5 and 413.2 eV correspond to Cd $3d_{5/2}$ and $3d_{3/2}$ binding energies. The S 2p peaks (Fig. 4e) at 162.1 and 163.5 eV are ascribed to S^{2-} in the 4d transition metal sulfide[43] and subjected to heterojunctional modification.[44] The Cu 2p peaks (Fig. 4f) at 935 eV can be assigned to Cu^{2+}. These results of XPS are also in accordance with the XRD, FTIR, SEM and TEM, which indicating the CuPW–CdS has successfully prepared.

Optical properties of semiconductor have significantly impact photocatalytic performance. In order to investigate the effect of CuPW for light absorption after loading CdS, optical properties of CuPW–CdS were measured by UV-vis DRS. The absorption edge of CuPW was analyzed at 420 nm, which was corresponding band gap of CuPW at 2.8 eV (Fig. S3†). Moreover, the absorption intensity increased with CdS load due to the visible absorption of CdS. From the optical measurement, it is found the CdS most probably distributes at the surface of CuPW, which is in accordance to the microscopic determinations. The nitrogen adsorption–desorption measurement was employed to study the specific surface areas (SSAs) and porosity of samples. Fig. S4† shows the nitrogen adsorption–desorption isotherms as well as the corresponding pore size distribution curve for CuPW–CdS samples. The SSA, pore volumes and pore size were listed in ESI at Table S2.† The samples exhibited IV isotherm, which is the typical characteristic of mesoporous materials. The SSA of CuPW–CdS-0, CuPW–CdS-5, CuPW–CdS-10 and CuPW–CdS-15 samples were 10.45 $m^2\ g^{-1}$, 13.02 $m^2\ g^{-1}$, 19.27 $m^2\ g^{-1}$ and 22.28 $m^2\ g^{-1}$ respectively. With increasing amounts of CdS, the SSA increased due to introduce CdS nanoparticles.

3.2 Photocatalytic results

The photocatalytic degradation experiment of TC under light irradiation was carried out to evaluate the photocatalytic performances of CuPW–CdS composites. Fig. 5a shows the degradation efficiencies of TC. Samples own different

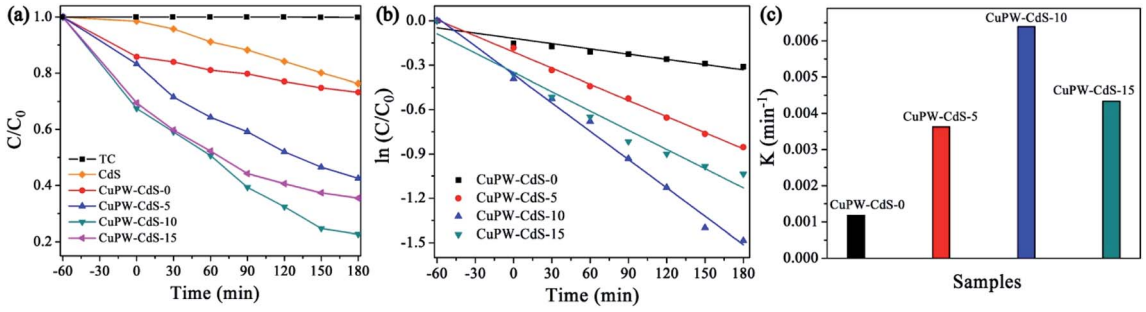

Fig. 5 Photocatalytic performance of as-prepared photocatalysts. (a) Photocatalytic degradation of TC. (b) Photodegradation kinetics of TC. (c) Comparison of the reaction rate constants of TC.

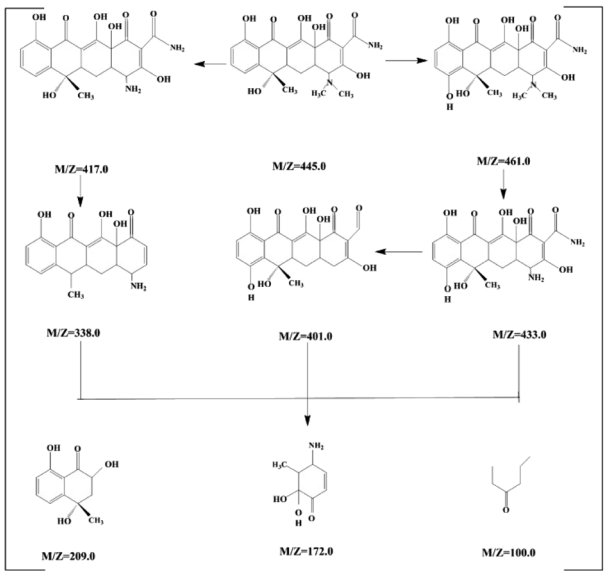

Fig. 6 Proposed degradation pathway of TC.

adsorption abilities of TC in the dark, which attributed to combinations of different pore size and SSAs. It's worth noting that CuPW–CdS-10 illustrated the higher adsorption efficiency of 21.9% for TC because of its mesoporous materials with largest pore size. To explore the adsorption ability of CuPW–CdS-10 sample, the adsorption experiments were carried out for different TC concentration under the dark. As shown in Fig. S5a,† the adsorption efficiency of TC molecules for CuPW–CdS-10 sample increased when the TC concentration increased from 5 to 15 mg L^{-1}, indicating that the adsorption–desorption capacity remains constant when the amount of catalyst is determined. It appears that CuPW–CdS-0 is less photocatalytic degradation efficient at about approximately 23%. The main reason is hardly separation of electrons and holes. After introduced with CdS, the photocatalytic efficiencies of CuPW–CdS composites have been improved significantly. CuPW–CdS-5 may remove ~57% TC of a less value after 180 min. The best photocatalytic activity is observed with CuPW–CdS-10 when degrading the TC (79% in 3 h) under visible light irradiation. Although the efficiency is lower than the recently reported 99.9% of Ag NPs confined in shell-in-shell hollow TiO_2 and 100% of SiO_2@TiO_2–Fe_2O_3 hollow spheres under simulated solar light irradiation,[45,46] it could be compared with the reported 75% in Z-scheme Ag_3PO_4/$CuBi_2O_4$ photocatalysts and even much higher than 71.2% by Ag_3VO_4/WO_3 photocatalyst reported.[47,48] Further increases of the content for CdS in the CuPW–CdS composites, however, would lead to the decrease of degradation efficiencies. CuPW–CdS-15 shows the photocatalytic degradation efficiencies of 65%. The degradation efficiencies of TC increased in the order of CuPW–CdS-0 (23%) < CuPW–CdS-5 (57%) < CuPW–CdS-15 (65%) < CuPW–CdS-10 (79%) under the same conditions.

Introduction of CdS enhances the photocatalytic activity of CuPW, but only at certain amount to have best photocatalytic performance. This can be explained as follows: (i) excessive CdS restricts light absorption through shield the incident light, which inhibits the production of active radicals. (ii) Light harvesting competes between surface active sites and compositions for photocatalytic degradation.[49] In order to better understand the speed of TC degradation, the degradation kinetics of TC was calculated by pseudo-first-order equation (in Fig. 5b and c). The rate constants of were calculated to be 0.00118, 0.00363, 0.00639 and 0.00434 min^{-1} for the samples. The value of CuPW–CdS-10 is about 6 times higher than that of CuPW–CdS-0, indicating remarkably enhanced photocatalytic performance of CuPW by loading CdS.

The toxicity of intermediate and final products was studied. The products of tetracycline were identified by mass spectroscopy (MS) in Fig. S6.† It shown that nine new peaks appeared at the reaction time of 90 minutes with *m*/*z* of 445.0, 461.0, 433.0, 417, 401.0, 338, 209, 172 and 100.[50] According to the MS results, we can deduce the possibly intermediates of TC attacked by superoxide radical. TC would be degraded to dehydroxylation, deamination and ring opening reaction, and degraded to low-molecular. Following the molecular determination, as shown in Fig. 6, the possible degradation pathway of tetracycline was proposed.

In order to widely application, the photocatalytic degradation of RhB was also carried out except to TC. Fig. 7a and S5b† show that 60 min is needed to reach the adsorption equilibrium of RhB on the photocatalysts in the dark. Therefore, the RhB solution and photocatalyst were successively stirred for 60 min in the dark to establish the adsorption equilibrium before the

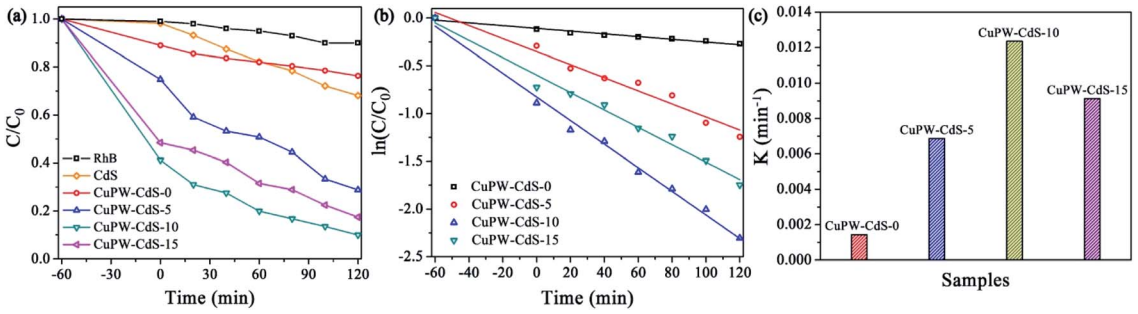

Fig. 7 Photocatalytic performance of as-prepared photocatalysts. (a) Photocatalytic degradation of RhB. (b) Photodegradation kinetics of RhB. (c) Comparison of the reaction rate constants of RhB.

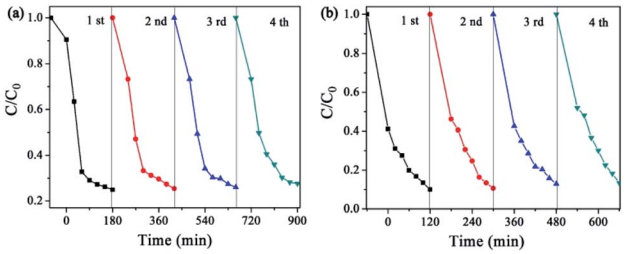

Fig. 8 The stability and reusability of (a) TC and (b) RhB.

degradation experiments. CuPW–CdS-10 also exhibited the best photocatalytic removal of RhB at a high efficiency of 91% in Fig. 7a. Meanwhile, the degradation efficiencies of the CuPW–CdS-5 and CuPW–CdS-15 were 71% and 83%, respectively. The RhB removal trend is in line with the TC result. Similar kinetics was also studied for the RhB degradation process. The pseudo-first-order reaction kinetics was 0.00639 min^{-1} for CuPW–CdS-10 (Fig. 7b and c). It is interesting that the photocatalytic activity of CuPW–CdS composites on RhB is higher than that of TC. This may result from the different stabilities of two pollutants: the higher stability of TC filled the center of photocatalyst active sites, which lead to the inhabitation of photodegradation. Furthermore, the apparent rate constants of TC degradation on CuPW–CdS composites are lower than that of RhB.

The reusability tests of the photocatalysts (CuPW–CdS-10) were carried out. The photocatalytic activity was no remarkably decrease after four cycles in Fig. 8, which demonstrating the superior chemical stability of the photocatalyst. For direct observation photocatalytic recyclability, the photocatalytic degradation data is described using the pseudo-first-order equation in Fig. S7.† According to the equation, the photocatalytic degradation constants of every reusability test were calculated to be nearly equivalent for CuPW–CdS-10. Furthermore, the XRD patterns of CuPW–CdS-10 before and after reactions were also displayed in Fig. S8.† There were no impurity peaks that appeared in the CuPW–CdS-10 samples after four cycles. As a result, it is shown that the combination of CuPW and CdS not only solve the defects of $H_3PW_{12}O_{40}$ visible light response and soluble, but also can avoid the photocorrosion of CdS.

The results also prove the solution to the problems of visible light response and soluble of $H_3PW_{12}O_{40}$ and the photocorrosion of CdS.

3.3 Photocatalytic mechanism

The charge transfer and separation procedures were investigated through combined results of the PL, photocurrent and EIS measurements. In Fig. 9a, the PL emission peak of samples locates at 530 nm and CuPW–CdS-0 gives the highest intensity. This peak diminishes with the CdS quantity. The CuPW–CdS-10 emits the least number of photons compared with CuPW–CdS-5 and CuPW–CdS-15. The recombination of electron–hole pairs *via* optical transition was remarkably prohibited.

To verify the charge transfer of CuPW–CdS composites, the photocurrent and EIS characterizations of CuPW–CdS-0, CuPW–CdS-5, CuPW–CdS-10, CuPW–CdS-15 were investigated and shown in Fig. 9b and c. The CuPW–CdS-0 exhibits a negligible photocurrent responds, attributing to the sluggish charge transfer and heavily charge recombination. However, the photocurrent of CuPW–CdS-10 was about 10 times higher than CuPW–CdS-0, demonstrating the higher electron–hole pairs separation ability on CuPW–CdS-10. Moreover, the EIS Nyquist plot of CuPW–CdS-10 owns the smallest radius compared with CuPW–CdS-0, CuPW–CdS-5 and CuPW–CdS-15. The charge recombination is substantially inhibited on the CuPW–CdS-10.[51] PL, photocurrent and EIS are well consistent with the result of photocatalytic degradation experiment.

To further investigate the formation of $^{\bullet}O_2^-$ and $^{\bullet}OH$ active species, ESR spectroscopy was carried out with DMPO in methanol and H_2O as a spin trap to capture $^{\bullet}OH$ and $^{\bullet}O_2^-$. As depicted in Fig. 10, the strong characteristic peaks of DMPO–$^{\bullet}O_2^-$ was obviously observed under visible light irradiation while the weak signal was detected in dark. However, the peaks of DMPO–$^{\bullet}OH$ was weak light irradiation, which indicating a few number of $^{\bullet}OH$ has been produced. Here, ESR results confirm that $^{\bullet}O_2^-$ radicals are mainly active species during the photodegradation process, in accordance to the scavenger quenching results (Fig. S9†).

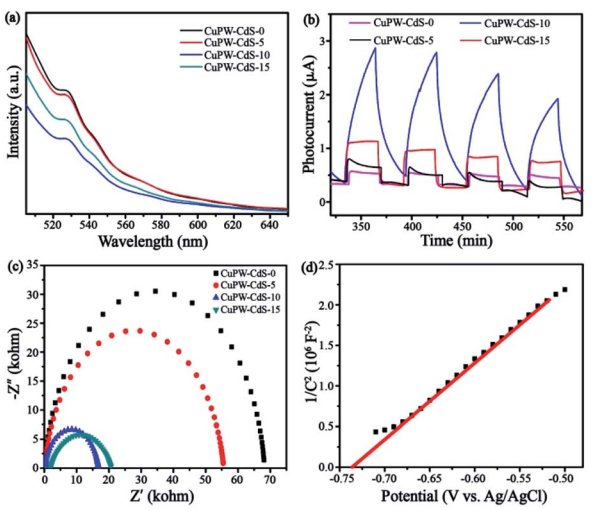

Fig. 9 (a) PL spectra of samples. (b) Transient photocurrent response of samples under visible light. (c) EIS Nyquist plots of samples. (d) The Mott–Schottky plots of CuPW.

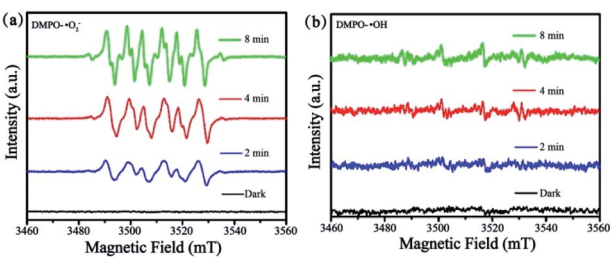

Fig. 10 ESR spectra of CuPW–CdS-10: (a) DMPO–$^{\bullet}O_2^-$ and (b) DMPO–$^{\bullet}OH$.

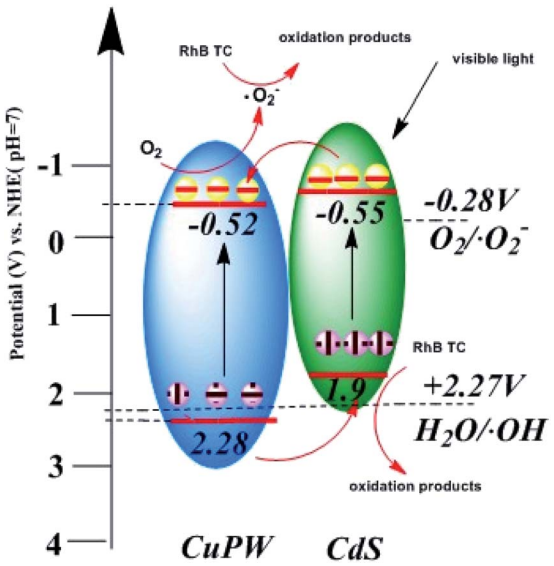

Scheme 1 The photocatalytic mechanism for CuPW–CdS composite photocatalysts.

In Fig. 9d, according to Mott–Schottky equation, the flat-band positions of CuPW can be determined. The straight upward curves demonstrate that CuPW is an n-type semiconductor and the CB of CuPW was calculated by Nernst equation.[52] Hence, the measurement of CuPW's CB level is *ca.* −0.48 V (*vs.* NHE) and the calculation of its VB level is *ca.* 2.31 V (*vs.* NHE). It is known that CdS's CB and VB levels are *ca.* −0.55 and 1.9 V (*vs.* NHE), respectively.

Following the above evidences, the photocatalytic mechanism was derived and proposed in Scheme 1. Under visible-light irradiation, CuPW and CdS are both actively produce photogenerated electron–hole pairs. In general, the conduction band of CuPW is lower than CdS so that electrons of CdS transfer to the CB of CuPW. Meanwhile, $\cdot O_2^-$ was produced from the reduction of adsorbed O_2 in CB of CuPW, which have powerful oxidative activity to degrade RhB and TC. However, the VB levels of CdS are not positive enough so that it doesn't have sufficient oxidation ability to drive the oxidation process. The CuPW has higher VB levels which can oxide H_2O to form $\cdot OH$. The comparison of $\cdot OH/H_2O$ potential (*ca.* 2.27 V) suggests that photogenerated holes (h^+) in the VB of CuPW transfer to the VB of CdS. This explains the significance of $\cdot OH$ in the photocatalytic performance. It can be concluded that the photocatalytic reaction in the presence of CuPW–CdS composites following this mechanism. The pair of photogenerated electron–hole separate and transfer quickly within the hetero parts. A more productive degradation of TC and RhB happens at the same time because of the potent oxidation capacity and reduction abilities form migrated electrons compensate charge loss of the CdS, leading to the overall chemical stability of the composites.

4. Conclusions

In conclusion, we have successfully modified phosphotungstic acid with macrocyclic Cu(II) to endow a visible photocatalytic ability in the composites. The CuPW–CdS heterojunctions were synthesized through a facile precipitation method. The robust photocatalytic activity have been shown in decontaminating the medical pollutant TC and model dye of RhB. Chemical stability has also been reached for the synthesized composites. The optimized CdS load is identified at 10 wt% where both TC and RhB removal efficiency peak. The charge transfer schemes were revealed and employed to study photocatalytic mechanism. It was found that charge migrations within the CuPW and CdS promote reaction radical generation, while compensate charge loss. As a result, the photocatalytic ability and chemical stability are enhanced. Beside the guidance for the widely application of phosphotungstic acid, the work serves a physical mechanism of charge compensation in the heterojunctional catalysts that will help future photocatalyst designs in practical detoxification for medical pollutants.

Conflicts of interest

There are no conflicts to declare.

Acknowledgements

The authors acknowledge with thanks the financial support of Hunan 2011 Collaborative Innovation Center of Chemical Engineering & Technology with Environmental Benignity and Effective Resource Utilization and the National Natural Science Foundation of China (51965009; 21343008), Science and Technology Plan Project of Guizhou Province: [2019]5616. Feng Li thanks the support of China Scholarship Council.

Notes and references

1 R. Daghrir and P. Drogui, *Environ. Chem. Lett.*, 2013, **11**, 209–227.
2 D. Wang, F. Jia, H. Wang, F. Chen, Y. Fang, W. Dong, G. Zeng, X. Li, Q. Yang and X. Yuan, *J. Colloid Interface Sci.*, 2018, **519**, 273–284.
3 S. Wu, H. Hu, Y. Lin, J. Zhang and Y. Hu, *Chem. Eng. J.*, 2020, **382**, 122842.
4 H. Kim, Y. S. Hwang and V. K. Sharma, *J. Chem. Eng.*, 2014, **255**, 23–27.
5 K. C. Khulbe and T. Matsuura, *Appl. Water Sci.*, 2018, **8**, 19.
6 N. B. Saleh, A. Khalid, Y. H. Tian, C. Ayres, I. V. Sabaraya, J. Pietari, D. Hanigan, I. Chowdhury and O. G. Apul, *Environ. Sci.: Water Res. Technol.*, 2019, **5**, 198–208.
7 X. X. Qiao, G. F. Liu, J. T. Wang, Y. Q. Zhang and J. Lü, *Cryst. Growth Des.*, 2020, **20**, 337–344.
8 G. Ghosh, S. Hanamoto, N. Yamashita, X. Huang and H. Tanaka, *Pollution*, 2016, **2**, 131–139.
9 C. N. Reddy, S. Bae and B. Min, *Bioresour. Technol.*, 2019, **285**, 121328.
10 M. Yan, Y. Hua, F. Zhu, L. Sun, W. Gu and W. Shi, *Appl. Catal., B*, 2017, **206**, 531–537.
11 H. B. Huang, N. Zhang, K. Yu, Y. Q. Zhang, H. L. Cao, J. Lü and R. Cao, *ACS Sustainable Chem. Eng.*, 2019, **7**, 16835–16842.

12 H. B. Huang, K. Yu, J. T. Wang, J. R. Zhou, H. F. Li, J. Lü and R. Cao, *Inorg. Chem. Front.*, 2019, **6**, 2035–2042.
13 Z. M. Qiang, S. W. Zhu, T. H. Li and F. Li, *Mater. Today Commun.*, 2020, 100980.
14 S. Li, S. Hu, J. Zhang, W. Jiang and J. Liu, *J. Colloid Interface Sci.*, 2017, **497**, 93–101.
15 H. B. Huang, Y. Wang, W. B. Jiao, F. Y. Cai, M. Shen, S. G. Zhou, H. L. Cao, J. Lü and R. Cao, *ACS Sustainable Chem. Eng.*, 2018, **6**, 7871–7879.
16 H. B. Huang, Y. Wang, F. Y. Cai, W. B. Jiao, N. Zhang, C. Liu, H. L. Cao and J. Lü, *Front. Chem.*, 2017, **5**, 123.
17 X. M. Ma, Z. Ma, T. Liao, X. H. Liu, Y. P. Zhang, L. L. Li, W. B. Li and B. R. Hou, *J. Alloys Compd.*, 2017, **702**, 68–74.
18 A. Meng, L. Zhang, B. Cheng and J. Yu, *Adv. Mater.*, 2019, **31**, 1807660.
19 Q. Shi and J. Ye, *Angew. Chem., Int. Ed.*, 2020, **59**(13), 4998–5001.
20 Z. M. Qiang, J. Q. Huang, C. Y. Yang, F. Li, T. H. Li, M. Huttula, Z. J. Huang and W. Cao, *J. Inorg. Organomet. Polym.*, 2019, 1–10.
21 C. Y. Wang, X. Zhang, H. B. Qiu, G. X. Huang and H. Q. Yu, *Appl. Catal., B*, 2017, **205**, 615–623.
22 D. Jiang, T. Wang, Q. Xu, D. Li, S. Meng and M. Chen, *Appl. Catal., B*, 2017, **201**, 617–628.
23 S. Chen, M. Zhou, T. Li and W. Cao, *J. Mol. Liq.*, 2018, **272**, 27–36.
24 Z. Wang, C. Li and K. Domen, *Chem. Soc. Rev.*, 2019, **48**, 2109–2125.
25 L. Zhou, J. M. P. Martirez, J. Finzel, C. Zhang, D. F. Swearer, S. Tian, H. Robatjazi, M. H. Lou, L. L. Dong, L. Henderson, P. Christopher, E. A. Carter, P. Nordlander and N. J. Halas, *Nat. Energy*, 2020, **5**, 61–70.
26 P. Kögerler, B. Tsukerblat and A. Müller, *Dalton Trans.*, 2010, **39**, 21–36.
27 E. Hampson, J. M. Cameron, S. Amin, J. Kyo, J. A. Watts, H. Oshio and G. N. Newton, *Angew. Chem., Int. Ed.*, 2019, **58**, 18281–18285.
28 H. F. Shi, Y. C. Yu, Y. Zhang, X. J. Feng, X. Y. Zhao, H. Q. Tan, S. U. Khan, Y. G. Li and E. B. Wang, *Appl. Catal., B*, 2018, **221**, 280–289.
29 W. L. Sun, B. W. An, B. Qi, T. Liu, M. Jin and C. Y. Duan, *ACS Appl. Mater. Interfaces*, 2018, **10**, 13462–13469.
30 L. Li, C. Zhang and W. Chen, *Nanoscale*, 2015, **7**, 12133–12142.
31 W. D. Peng, C. Yang and J. Yu, *RSC Adv.*, 2020, **10**, 1181–1190.
32 J. Yu, Y. Yu, P. Zhou, W. Xiao and B. Cheng, *Appl. Catal., B*, 2014, **156**, 184–191.
33 H. Yu, X. Huang, P. Wang and J. Yu, *J. Phys. Chem. C*, 2016, **120**, 3722–3730.
34 Y. Chen, F. Li, W. Cao and T. Li, *J. Mater. Chem. A*, 2015, **3**, 16934–16940.
35 P. Wang, H. Li, Y. Sheng and F. Chen, *Appl. Surf. Sci.*, 2019, **463**, 27–33.
36 J. Jin, J. Yu, D. Guo, C. Cui and W. Ho, *Small*, 2015, **11**, 5262–5271.
37 L. Qiu, X. Qiu, P. Li, M. Ma, X. Chen and S. Duo, *Mater. Lett.*, 2020, 127566.
38 S. Q. Chen, F. Li, T. H. Li and W. Cao, *J. Colloid Interface Sci.*, 2019, **547**, 50–59.
39 P. Qiu, H. Chen and F. Jiang, *RSC Adv.*, 2014, **4**, 39969–39977.
40 I. H. Antunović, D. B. Bogdanović, A. Popa, V. Sasca, B. N. Vasiljević, A. Rakić and S. U. Marković, *Mater. Chem. Phys.*, 2015, **160**, 359–368.
41 J. J. Tian, L. X. Zhang, X. Q. Fan, Y. J. Zhou, M. Wang, R. L. Cheng, M. L. Li, X. T. Kan, X. X. Jin, Z. H. Liu, Y. F. Gao and J. L. Shi, *J. Mater. Chem. A*, 2016, **4**, 13814–13821.
42 W. Cao, V. Pankratov, M. Huttula, X. Shi, S. Saukko, Z. Huang and M. Zhang, *Mater. Chem. Phys.*, 2015, **158**, 89–95.
43 K. Gelderman, L. Lee and S. W. Donne, *J. Chem. Educ.*, 2007, **84**, 685.
44 S. Sakthivel and H. Kisch, *Angew. Chem., Int. Ed.*, 2003, **42**, 4908–4911.
45 S. D. Zhao, J. R. Chen, Y. F. Liu, Y. Jiang, C. G. Jiang, Z. L. Yin, Y. G. Xiao and S. S. Cao, *Chem. Eng. J.*, 2019, **367**, 249–259.
46 S. Zhang, J. J. Yi, J. R. Chen, Z. L. Yin, T. Tang, W. X. Wei, S. S. Cao and H. Xu, *Chem. Eng. J.*, 2020, **380**, 122583.
47 M. Yan, Y. L. Wu, F. F. Zhu, Y. Q. Hua and W. D. Shi, *Phys. Chem. Chem. Phys.*, 2016, **18**, 3308–3315.
48 W. L. Shi, F. Guo and S. L. Yuan, *Appl. Catal., B*, 2017, **209**, 720–728.
49 Y. Hu, X. Q. Hao, Z. W. Cui, J. Zhou, S. Q. Chu, Y. Wang and Z. G. Zou, *Appl. Catal., B*, 2020, **260**, 1181311.
50 H. Guo, C. G. Niu, L. Zhang, X. J. Wen, C. Liang, X. G. Zhang, D. L. Guan, N. Tang and G. M. Zeng, *ACS Sustainable Chem. Eng.*, 2018, **6**, 8003–8018.
51 Z. M. Qiang, X. M. Liu, F. Li, T. H. Li, M. Zhang, H. Singh, M. Huttula and W. Cao, *Chem. Eng. J.*, 2021, **403**, 126327.
52 A. Fujishima and X. Zhang, *C. R. Chim.*, 2006, **9**, 750–760.